Draft version July 22, 2025
Typeset using LaTeX **twocolumn** style in AASTeX631

arXiv:2507.15834v1 [astro-ph.GA] 21 Jul 2025

SDSO1 is a Ghost Planetary Nebula Bow Shock in Front of M31

Patrick Ogle,[1,2] Mark Petersen,[2] Tim Schaeffer,[3] Lewis McCallum,[4] Alberto Noriega-Crespo,[1] R. Michael Rich,[5,2] Biny Sebastian,[1] Carl Björk,[6] Steeve Body,[7] Sendhil Chinnasamy, Marcel Drechsler, Tarun Kottary, Yann Sainty, Patrick Sparkman, and Xavier Strottner

[1] *Space Telescope Science Institute, 3700 San Martin Drive, Baltimore, MD 21218, USA*
[2] *Polaris Imaging, CA, USA*
[3] *Delft University of Technology, The Netherlands*
[4] *University of St. Andrews*
[5] *Dept. of Physics and Astronomy, University of California, Los Angeles, PAB 430 Portola Plaza 90095-1547*
[6] *EPFL, Switzerland*
[7] *Griffith University, Brisbane, Queensland, Australia*

ABSTRACT

We present new, deep narrowband imagery and discuss the nature of SDSO1, the large [O III]-emitting nebula centered 1.5° SE of M31. We find strong evidence to support the hypothesis that SDSO1 is unrelated to M31 and is instead a bow shock driven by a faded, giant ($D = 20$ pc), 400 kyr-old, ghost planetary nebula (GPN) expelled by the symbiotic WD binary star EG Andromedae. Because EG And lags the rotation of the Milky Way, its hypersonic velocity of 107 km s^{-1} drives a shock into the local interstellar medium. SDSO1 also sports a 45-pc long turbulent tail that crosses M31. We establish the shock-powered GPN phase as a new phase of PN evolution, and identify seven more candidate GPNe by their large size and shock-tail morphology. This includes several giant halos of younger planetary nebulae, possibly expelled by now degenerate binary companions. The interaction of an old, fast-moving GPN with the ISM generates a shock that remains visible long after the photoionized PN shell has faded below the limit of detectability. The SDSO1 GPN has reached a phase in its evolution where its outward expansion has been slowed considerably by the work it has done on the interstellar medium. Once the GPN outflow expends the rest of its kinetic energy, it will be stripped from EG And and mix into the surrounding ISM.

Keywords: Planetary nebula () — Shock () — Interstellar medium ()

1. INTRODUCTION

Planetary nebulae give unique insights into both single and binary star stellar evolution, completing the cycle of low-mass star birth, death and return of elements to the interstellar medium (ISM). The interaction of planetary nebulae with the ISM informs our knowledge of both the ISM and shock physics. There are several known examples of fast-moving planetary nebulae with distorted shells or bow shocks and tails indicative of PN-ISM interaction (Borkowski et al. 1990; Tweedy & Kwitter 1996). Sophisticated models of these systems with hydrodynamic codes reproduce crucial features (Soker et al. 1991; Wareing et al. 2007a; Chiotellis et al. 2016). As we will show, PN-ISM interactions also present the opportunity to find and study otherwise undetectable old planetary nebulae by their shocks and tails. The late-stage evolution of planetary nebulae is difficult to observe because they fade rapidly as they expand (Jacob et al. 2013). The study of of large planetary nebulae (PNe) at optical wavelengths, from a few arcminutes to degrees across the sky, has a long tradition (e.g., Tweedy & Kwitter 1994, 1996). One of the closest examples , Sh 2-216 at 120 pc, covers as much as 1.6° in diameter (Tweedy et al. 1995). The oldest known planetary nebula IPHASXJ055226.2 +323724 has a diameter of 3 pc and kinematic age of 70 kyr (Fragkou et al. 2022).

Deep [O III] λ5007 Å observations of M 31 and environs by amateur astrophotographers recently revealed a giant nebular arc 1.5° SE of the galaxy, cataloged as SDSO1 (Drechsler et al. 2023; Fesen et al. 2023). The uncertain origins of SDSO1 were debated, whether foreground in our own Galaxy, or directly related to M 31. Based on its large angular size, Fesen et al. (2023) ruled out SDSO1 as a planetary nebula. Furthermore, they found its location above the Galactic plane and unusual

structure to be inconsistent with known Galactic supernova remnants. They considered and rejected the possibility of a bow shock nebula related to a high-velocity massive star, red giant, or AGB star. Because of its large radial velocity ($\sim$ -100 km s^{-1}), EG Andromedae was considered a likely target to develop a bow shock structure, as documented in the IRA/ISSA Survey study by van Buren et al. (1995). Surprisingly at the time, the lack of warm dust was difficult to explain with the classical photoionized wind model (Kenyon & Garcia 2016). Fesen et al. (2023) searched the area near SDSO1 for white dwarfs (WD), but found none that could fit the bill as a planetary nebula central star. In particular, they noted that EG Andromedae is the second-brightest UV source in the region. However, its 608 ± 12 pc distance (based on Gaia parallax) would imply a diameter of 20.0 ± 0.4 pc for SDSO1, which they found unlikely for a planetary nebula.

Fesen et al. (2023) favor the explanation that SDSO1 is an extragalactic shock associated with M31, even though they recognize that its radial velocity of -10 km s^{-1} is inconsistent with the -297 km s^{-1} radial velocity of M31. They also suggest that SDSO1 is associated with stellar tidal streams. Large broad band surveys of M31, like the "Pan-Andromeda Archelogical Survey" (PAndAS) do suggest the presence of other large emission features besides the well known stellar tidal streams (McConnachie et al. 2009, see, e.g., Fig. 1). However, narrow band observations are necessary to distinguish the gas emission features from the broad band continuum dominated by the stellar light. Furthermore, high resolution spectroscopy yields an intrinsic emission line FWHM of < 19 km s^{-1}, disfavoring an extragalactic shock and instead pointing to a Galactic origin (Lumbreras-Calle et al. 2024).

We present compelling evidence that SDSO1 is actually a bow shock driven by a very large GPN moving hypersonically through the interstellar medium (ISM) of the Milky Way. We also identify several other known very large [O III]-emitting nebulae and PNe giant halos as candidate GPN bow shocks. We present new narrow band imaging observations of SDSO1 in Section 2. We detail the properties of SDSO1 in Section 3, and its discuss its origins, dynamics, energetics, and evolution in §4.

2. NARROWBAND IMAGING OBSERVATIONS AND DATA REDUCTION

We observed SDSO1 and its environs (including M31, M 32, and NGC 205) in narrowband [O III] λ5007$\AA$, Hα, and broadband R, G, and B filters (Table 1). Our deep narrowband imaging relies on long (10–30 min) exposures and CMOS sensors on high-quality refracting telescopes to accumulate enough photons to beat the readout noise. Such long exposures also require stable mounts and capable guiding systems to take advantage of the best seeing conditions. Each of five astrophotographers utilized a Takahashi FSQ 106 mm (4-inch) refractor and focal reducer to achieve fast imaging at f/3.6 or f/3. This setup provided a wide field of view (3.5-5 degrees) covering the full extent of SDSO1 and the disk of M31. The telescopes were equipped with cooled, monochrome cameras with sensitive Sony CMOS sensors. Observations made during the 2024 September - December season netted a total integrated exposure time of 525 hr, after culling bad frames that didn't meet our acceptance criteria. This includes 313 hr of exposure in the [O III] band and 148 hr of exposure in the Hα band.

In order to explore additional fine details in SDSO1, including data in the [S II] λ6723$\AA$ band, we also present imaging over a narrower field obtained by the Deep Sky Collective for its 1000-Hour Project (released in March 2024). The equipment and integrated exposure times are listed in Table 1. This project utilized 15 telescopes with apertures ranging from 80-203 mm (3–8 inches) in diameter, obtaining 488 hr of exposure in the [O III] band, 314 hr in Hα, and 169 hr in [S II]. We utilize similar datasets for GPN candidates PN A66 15 and Hewett 1, courtesy of the NHZ collaboration and Bray Falls, respectively, so we can compare them to SDSO1.

Basic data reduction utilized the PixInsight software suite to align, stack, and integrate the data frames. Frames demonstrating large stellar eccentricity (> 0.7), stellar FWHM > 6", or large median flux indicative of clouds were rejected from the integration. The Generalzed Extreme Studentized Deviate (ESD) algorithm was used to reject outliers. The data frames were then optimally weighted using a custom weighting function that incorporated both S/N and stellar PSF quality metrics. Because the orientation and field of view of each wide field setup was different, extra care was taken to remove gradients using linear spline fitting functions and matching background levels at frame overlaps.

We employed our broadband R observations to estimate and subtract the continuum emission at Hα and [S II]. Because the wavelength dependence of galaxy stellar continuum is relatively weak in the R-band, the resulting continuum subtraction is quite robust to differences in stellar populations. The [O III] band continuum subtraction on the other hand is not as clean with a single band or even a constant linear combination of the B and G bands, which flank the line. We therefore devised a new algorithm, which we call Color Continuum

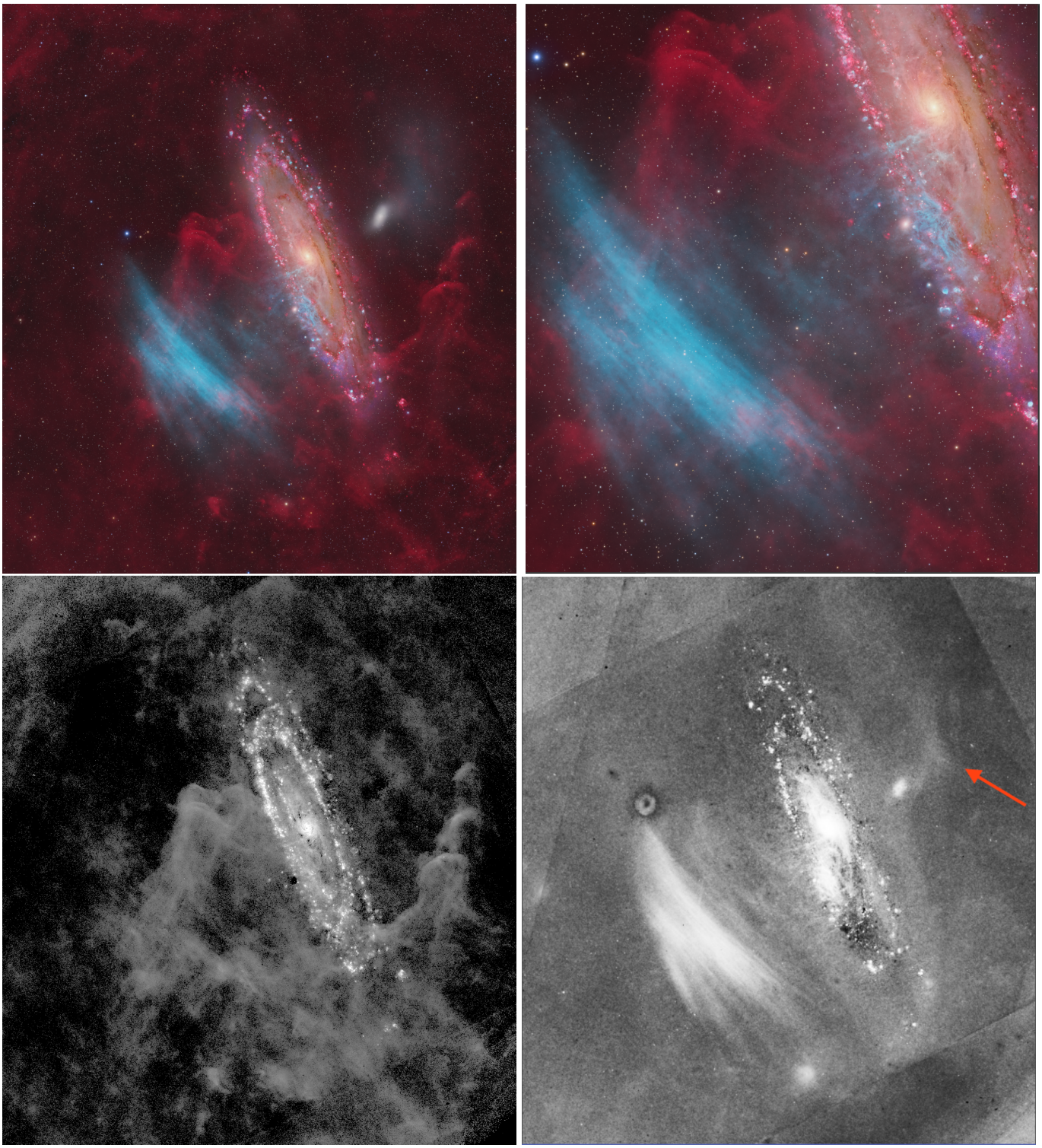

Figure 1. Our RGB and Narrow-band imaging of SDSO1, M31, M32, and NGC 205. Top: Hα and [O III] (HOO) plus RGB combination. Bottom Left: Continuum-subtracted Hα, with stars removed, using a logarithmic stretch. Bottom right: starless, continuum-subtracted [O III] with a hard logarithmic stretch to show the faintest features. The counter-arc location is indicated by the arrow.

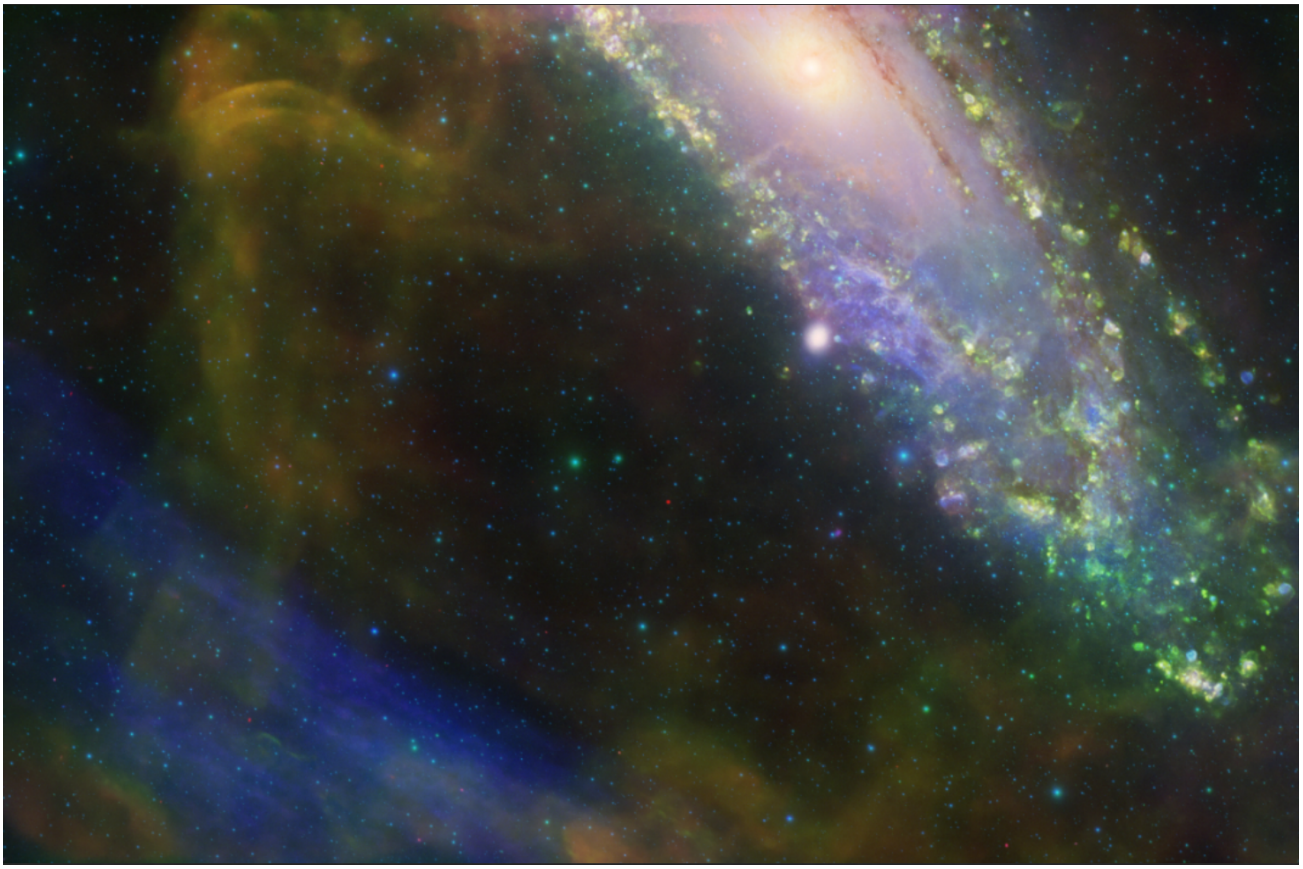

Figure 2. Narrow-band (r, g, b = [S II], Hα, [O III]) plus LRGB imaging of a portion of SDSO1, M31, and M32. Credit: Deep Sky Collective.

Subtraction (CCS), to better estimate the [O III] band continuum by logarithmically interpolating the continuum between the B and G bands in each pixel of our images. We dedicated extra imaging time to the B band, which is generally fainter than G against a greater sky background, in order to minimize the noise in our $B-G$ color estimate. CCS assumes the following simple linear equation in magnitude space:

$$O_{\rm cont}[mag] = G_{\rm cont}[mag] + a + b(B-G)_{\rm cont} \qquad (1)$$

This log-linear color relation is calibrated against the (dust-reddened) stellar population colors in M31, sampled in an aperture selected to contain both blue and red regions, but avoiding regions with nebular emission. O, G, and B image pixel values are extracted from the galaxy aperture, then the above relation is fit for its slope and intercept. The intercept contains information on the observing system relative response to photons in the 3 bands. The slope is related to the dust-reddened spectral energy distribution of the continuum and may in principal differ between different regions of a galaxy and between different galaxies. We further refined the continuum subtraction by separately fitting the CCS relation (Eqn. 1) for 3 different ranges of B-G, to account for small differences in intercept parameter a for the youngest and oldest stellar populations.

We calibrated our [O III], Hα and [S II] stellar photometry to g and r photometric catalog data from the Sloan Digital Sky Survey (SDSS). We then integrated the filter transmission curves to determine the filter equivalent widths for the emission line flux calibration.

3. RESULTS

Our deep images (Figs. 1 & 2) reveal many details in the nebular emission from SDSO1. The primary [O III] emission extends 1.7° and partially fills a circle of diameter $D_{\rm i} = 1.9°$ centered on EG And. The mean surface brightness is 1.9×10^{-17} erg s^{-1} cm^{-2} measured within the contour at 10% of the peak. Because there is no obviously visible PN shell, we adopt this as the approximate diameter for SDSO1. Fainter filaments are found within a circle of diameter $D_{\rm o} = 2.7°$ centered on EG And. A multitude of fine striations are present, grouped in several bundles that extend all the way to the disk of M31, in projection. We find emission from these striations in Hα and [S II] as well as [O III], with a strong positive correlation between the nebular emission seen in all three bands. Localized, bright Hα features also appear to be associated with the striations seen in [O III]. The [O III] luminosity of SDSO1, measured within the 10% surface brightness contour is 4.4×10^{33} erg s^{-1} ($2.4 L_{\odot}$).

Long, undulating, Hα-emitting structures appear to form in the wake of SDSO1, extending across and to the NW of M31. We suggest that this Hα tail is physically connected to SDSO1, providing crucial clues to its origin, motion, and evolution. These structures are often highlighted in deep Hα images of M31 and have in the past been attributed to non-specific, foreground Hα cirrus in the Milky Way. The brightest two features trailing from SDSO extend up to 3.0° from its leading edge (2.0° from EG And). The width of the wake, measured perpendicular to the proper motion vector of EG And, is comparable to the 1.9° [O III] diameter of SDSO1, providing a robust estimate of the size of the invisible PN shell. Additional wavy Hα and linear dust features, may extend as far as $2.9 - 4.3°$ from the head of SDSO1.

We detect a new [O III] - emitting structure trailing SDSO1, near NGC 205, that we dub the counter-arc, at a distance of $1.6 - 1.9°$ from EG And. This emission appears in two faint bands, separated by a band of Hα emission. The peak surface brightness of the counter-arc is only 9.6×10^{-19} erg s^{-1} cm^{-2}. We suggest that this is emission from the SDSO1 shock or tail, near the point of origin where the PN was initially ejected. Long, linear, possibly periodic Hα bands associated with the wake may mark dynamical instabilities associated with turbulence generated by the wake.

4. DISCUSSION

4.1. *SDSO1 is a Hypersonic GPN*

The morphology of SDSO1, relatively high surface brightness for its size, and association with the high-velocity WD binary EG And make it likely that a hypersonic bow shock driven by a ghost PN (GPN) is the primary source of the observed [O III] emission. As we demonstrate below, the line emission from WD photoionization is undetectable in the SDSO1 GPN shell and tail. Because they quickly expand and fade, following a $\sim t^{-3}$ density decrease (Soker et al. 1991; Jacob et al. 2013; Frew et al. 2016), observable PNe typically have diameters of < 1.5 pc and ages of $< 20,000$ years. However, older PNe may continue to grow to larger size and should be ubiquitous, but difficult to detect because of their low surface brightness. Together with morphological clues and central star identification, relatively high [O III] surface brightness is useful for distinguishing the new GPN class of PNe (Fig. 3). A GPN may identified by a shock-powered nebula with diameter $D > 3$ pc that is associated with a WD or hot subdwarf, and has a mean [O III] surface brightness more than 10 times as great as expected for its size, with respect to the trend followed by PNe. The temperature and surface brightness of the shock driven by a GPN into the ISM depends

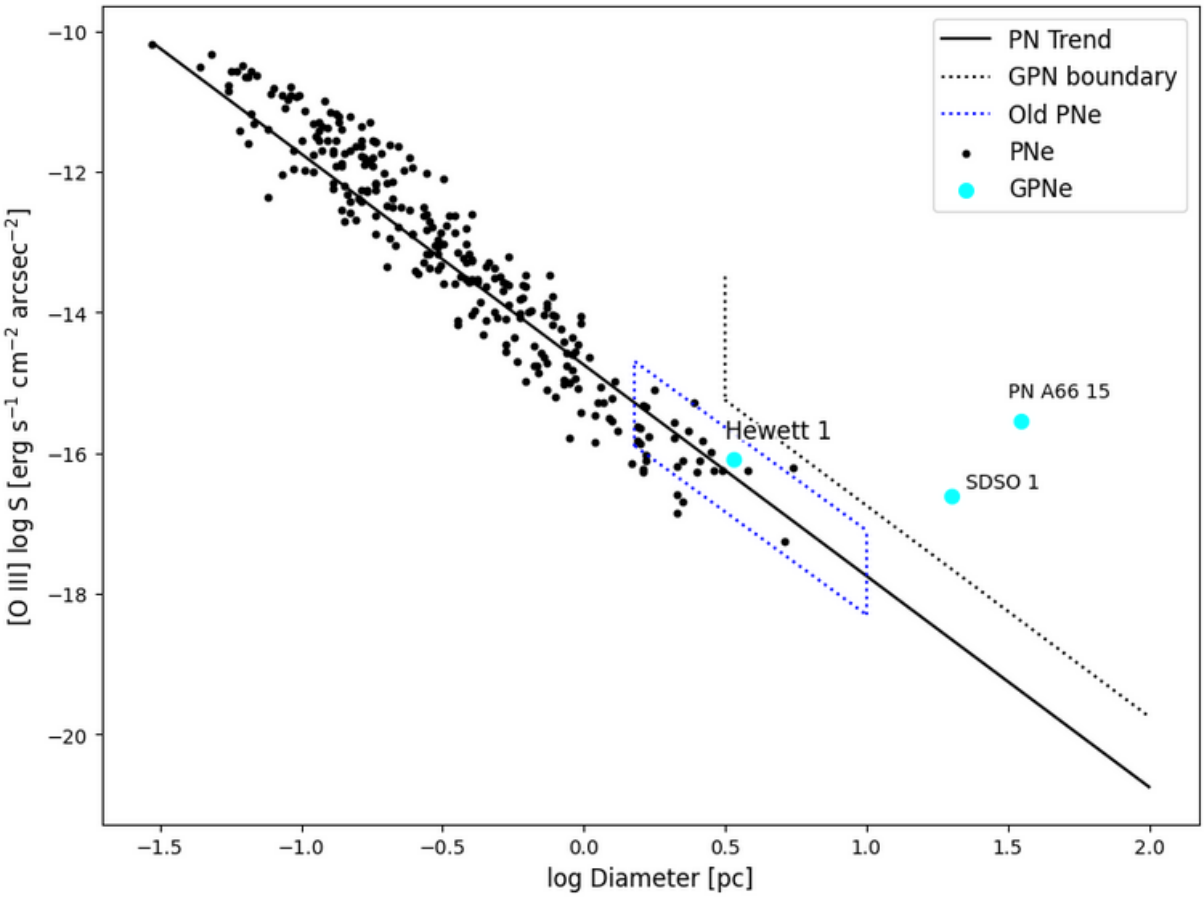

Figure 3. GPNe have high [OIII] surface brightness for their large size, compared to PNe. Mean PN surface brightness in [O III] is estimated from the compilation of Hα surface brightness by Frew et al. (2016) by assuming a typical Hα/[O III] value of 3.3. By convention, surface brightness and diameter are measured within a contour that is 10% of the peak surface brightness. Planetary nebula photoionized emission surface brightness declines with diameter as D^{-3} during the free expansion phase. GPN bow-shock nebulae with $>$ 10 times brighter [O III] emission above this trend are easily distinguished. Below a diameter of 3 pc, gas photoionized by the central star typically dominates the emission.

critically on both the surrounding gas density and its velocity through the ISM (Soker et al. 1991), so only the fastest GPNe will develop shocks that are visible in [O III]. While the GPN will initially retain its separate identity, once its outward expansion ceases it will be disrupted and stripped by ISM ram pressure, forming a long trail (§4.9). Fast-moving planetary nebulae in dense environments or encountering a dense cloud of gas may not survive to the shock-powered GPN stage (Ransom et al. 2015). Instead, they may be disrupted while they are still in a photoionization-dominated stage.

Because such a small fraction of the sky has been imaged to similar depth in [O III], SDSO1 is the first recognized GPN and one of only 8 GPN candidates that we have identified through a search of published images (Table 2). Its location near the famous nearby galaxy M31 led to deep imaging of the field and its serendipitous discovery. Considering planetary nebula expansion rates and evolution (Jacob et al. 2013), old PNe with $D = 3 - 30$ pc may be ten times more abundant than and cover 1000 times the sky area covered by $D < 3$ pc PNe. Sensitive surveys by both professional and amateur astronomers have revealed an increasing number of large, low-surface-brightness, old PNe (Table 2). The UV-bright central stars are either white dwarfs or hot sub-dwarfs. In many cases, the morphology consists of a central nebula with a leading arc-shaped shock front, surrounded by an elongated Hα envelope with a head-tail structure. This shock-tail morphology is a key indicator of motion through and interaction with the interstellar medium.

Three of the GPN candidates have comparable physical size to SDSO1. All of them have very clear [O III]-emitting bow shocks and tails that appear to be associated with the motion of a GPN through the ISM (Fig. 4). Six of the GPN candidates are giant halos of PNe that were previously thought to be diffuse ISM photoionized by EUV emission escaping the central PN (McCul-

Figure 4. GPNe and old PNe interacting with the interstellar medium. Top Left: GPN Alves 2 ($D = 16$ pc; credit: Randall Schleier 2025;https://app.astrobin.com/i/6rb2ww) may be an analogue to SDSO1. Top Right: The halo of PN A66 15 ($D = 35$ pc; credit: NHZ Team; https://app.astrobin.com/i/xrz3qx) may be an GPN + PN from a secondary WD. The strong shock on the right side and linear trailing features indicate fast motion through the ISM. Bottom Left: The shock-tail structure of HFG1 is apparent in this narrowband image (Credit: NOIRLab). Bottom Right: Hewett 1 (Hewett et al. 2003) is a large, old, interacting PN with shock-tail morphology, where the [OIII] emission is primarily from the shock, which wraps around the back of the mostly invisible PN, following the evolution of its expansion ($D = 3.4$ pc, credit: Bray Falls, 2025; https://app.astrobin.com/i/870jps).

lough et al. 2001). However, PN halos are typically much smaller, with $D < 1$ pc (Balick et al. 1992; Corradi et al. 2003). We therefore suggest that the largest PNe halos may be formed by GPNe ejected in a previous PN outflow associated with a secondary WD or Sd companion. Discovery of GPNe via deep narrowband imaging is is only possible where the emission is enhanced by ISM interaction (§4.5). GPNe that are moving slowly with respect to the ISM will remain invisible, with surface brightness much lower than the detection limit of existing [O III] surveys.

4.2. *The SDSO1 GPN Central Star EG Andromedae*

The eclipsing, S-type symbiotic WD binary star EG And (Wilson 1950) is very likely the SDSO1 GPN central star, for the following reasons. EG And is the second brightest GALEX FUV source in the region, after the much lower temperature (type-B5V) star ν And. EG And consists of a very hot (50,000 - 90,000 K) white

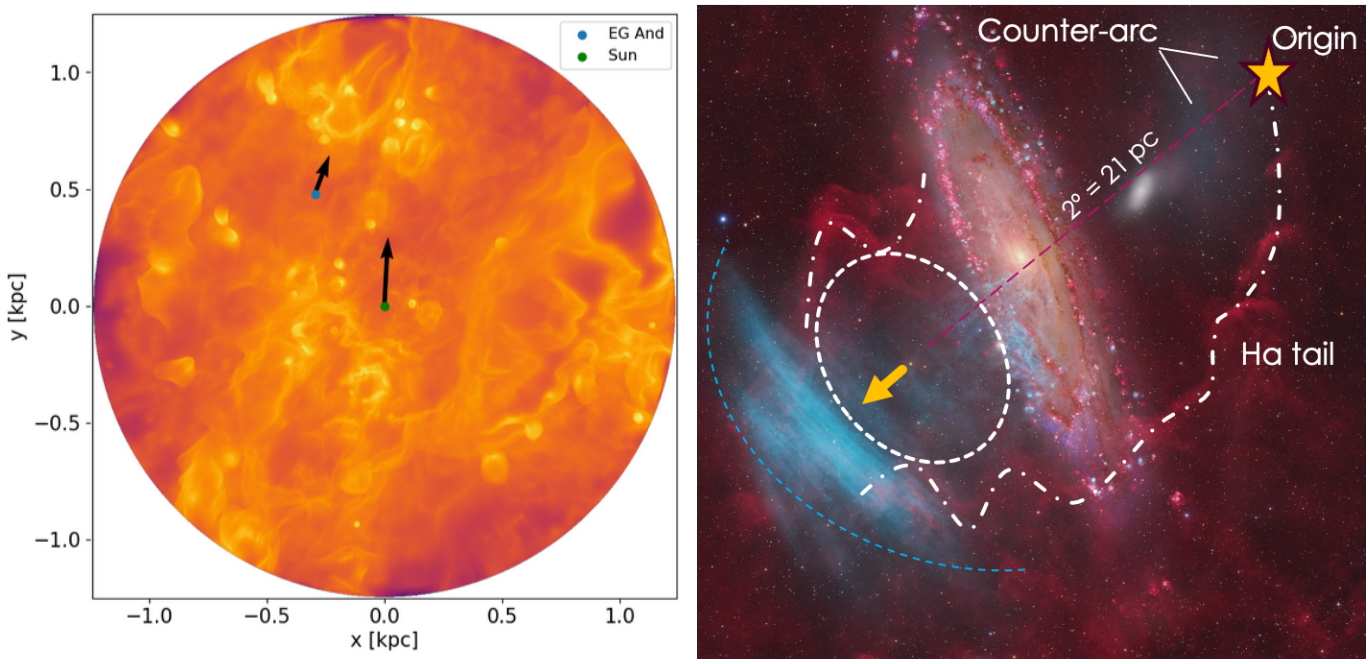

Figure 5. Left: Location and velocity of EG And relative to ionized gas in the local ISM, as mapped by McCallum et al. (2025). EG And lags the rotation of the Milky Way disk at a hypersonic velocity. Right: Sketch of EG And proper motion and the SDSO 1 GPN bowshock and tail, overlaid on our image.

dwarf with a mass of $0.35-0.55M_\odot$, orbiting a V=7.22 M2.4 III red giant with a mass of $1.1-2.4M_\odot$ (Kenyon & Garcia 2016). The parallax from Gaia is 1.65 ± 0.03 mas, indicating a distance of 608 ± 16 pc and a diameter of 20.0 ± 0.4 pc for SDSO1. Stellar luminosity estimates were initially made pre-Gaia, assuming a distance of 400 ± 20 pc, based on the properties of the red giant, including its radius measured from UV eclipses (Kenyon & Garcia 2016). We increase the luminosity estimates by a factor of 2.31 to the Gaia distance, yielding $L_h = 10-90L_\odot$ for the WD and $L_g = 2300-4600L_\odot$ for the red giant. Crucially, the proper motion vector of EG And: $(24.8 \pm 0.6, -44.6 \pm 1.1)$ km s^{-1} points towards SDSO1, consistent with a bow shock in this direction (Fig. 5).

It is important to consider the 3D location and velocity of EG And in order to understand how it can generate the SDSO1 bow shock. EG And is located -22 deg (208 pc) below the plane of the Milky Way and 295 pc outside of the solar circle, at a Galactic longitude of 122° (Fig. 5). The proper motion measured by Gaia is 51 ± 1 km s^{-1} in the plane of the sky. The radial velocity of the M giant component of EG And ranges from -87 to -103 km s^{-1}, depending on orbital phase, yielding a mean radial velocity of -95 km s^{-1} (Kenyon & Garcia 2016) and a velocity vector pointing $-28°$ along the line of sight. EG And therefore lags the rotation of the Milky Way and moves hypersonically with a velocity of 107 km s^{-1} (Mach 7.1) relative to the local ISM. Its velocity and location indicate that EG And is a runaway disk star with a highly elliptical orbit around the center of the Milky Way.

The mass and age of EG And, constrained by observations of its eclipses, tell us much about the WD progenitor star and the mass it shed to form the SDSO1 GPN. The relatively low masses of both the WD and red giant indicate low-mass progenitors, assuming that neither star was tidally stripped. However, the WD progenitor must have been slightly more massive than its M-giant companion so that it ended its time on the stellar main sequence first. Given that both stars recently (within the last 50 Myr) left the main sequence, then both the red giant and the WD progenitor must have begun as A or F dwarfs with masses of $1.1-2.4M_\odot$ and ages of $0.5-1.5$ Gyr. The amount of mass shed by the WD progenitor would then be $\sim 0.7-2M_\odot$.

4.3. *Density and ionization of the surrounding ISM*

We use the 3D map of ionized and neutral gas by McCallum et al. (2025) to characterize the properties of the ISM in the vicinity of EG And (Figs. 5 & 6). The map was constructed from the dust map of Edenhofer et al. (2024), and only considers ionizing photons from O stars, not B stars or WDs, so it does not consider the ionizing effects of EG And itself. EG And is located in a low-density ($n_e = 0.02$ cm^{-3}), ionized region above the Galactic plane, approaching a lane of neutral gas and associated ionization front which stretches across the field

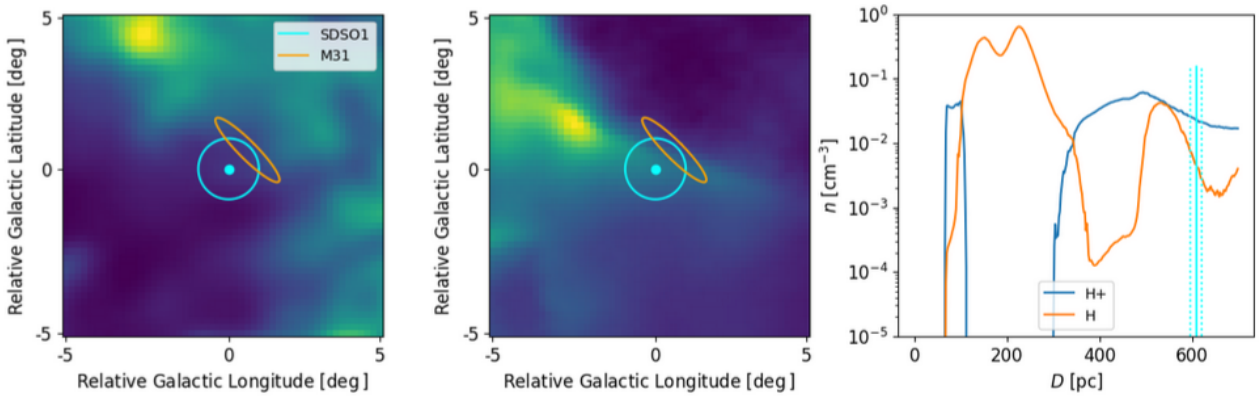

Figure 6. Density map of gas in the vicinity of SDSO1, extracted from the 3D map of McCallum et al. (2025). Left: Distribution of neutral gas in the plane of the sky. Center: ionized gas map. Right: distribution along the line of sight in a $2° \times 2°$ (40×40) pc^2 box centered on EG And.

of view of our image. While the density gradient in its direction of motion is increasing, it is shallow enough not to significantly effect the evolution of the GPN to this point. A larger region of neutral gas seen in the map is in the foreground, at a distance of 100-300 pc from the sun.

4.4. *The GPN Tail*

The Hα tail of the SDSO1 GPN is similar to those seen in fast-moving PNe such as HFG1 (Heckathorn et al. 1982; Boumis et al. 2009; Chiotellis et al. 2016). It likely derives from gas ablated from the PN surface by the Kelvin-Helmholtz instability from fast moving gas at the shock-PN interface (Soker et al. 1991; Scannapieco & Brüggen 2015). Dividing the projected length of the SDSO1 Hα tail by the projected velocity of EG And yields an estimated age of 400 kyr for the SDSO1 GPN. This estimate assumes that the full length of the GPN tail is still visible, which is supported by the apparent narrowing and convergence of the Hα tail at the counter-arc. It also assumes that the tail decelerates to the local ISM velocity on a timescale that is shorter than the age of the GPN. Otherwise, the length of the tail will be compressed and the age will be underestimated. Simulations of the AGB star Mira show that its tail may decelerate slowly, leading to an underestimate of its age (Wareing et al. 2007b).

EG And and its associated GPN are moving at Mach 7.1 relative to the surrounding ISM, assuming a sound speed of 15 km/s in $T = 1 \times 10^4$ K plasma. At that speed, the half opening angle of the Mach cone is expected to be $\theta_M = \arcsin 1/M = 8°$, with a projected angle on the plane of the sky of 16°. However, since the SDSO1 GPN grows comparably as fast as it advances in the plane of the sky, the geometry of the Hα tail does not look like a classical Mach cone. Instead, it wraps around the back of the PN and then converges towards the counter arc. This appears to be true for the other GPN candidates too (Fig. 4).

In addition to the broader Hα tail, a number of [O III]-emitting filaments appear to trail behind the SDSO1 GPN, between the location of EG And and the disk of M31 (Fig. 1). Many of these filaments continue halfway across the face of M31. It is difficult to tell if all of the filaments actually originate from the SDSO1 GPN or if some if them may be ejected from the disk of M31. We do expect to see such a tail behind the SDSO1 GPN, similar to the tail seen in Schlieren photographs of hypersonic spheres (Van Dyke 1982). A very prominent [O III] tail is similarly seen in GPN candidate Alves 2, and a fainter, yet very long and straight [O III] tail is found trailing behind the A55 15 PN (Fig. 4).

The [O III] emission from the feature that we call the counter-arc has never been detected before, and its origin is uncertain. Given that the counter-arc is so far removed from the head of SDSO1, it is surprising that it shows [O III] emission. It may be part of the bow shock that wraps around behind the expanding GPN shell. Similar broad [O III] tails (shaped like backswept wings) are found in GPNe candates Alves 2, the A66 15 PN halo, and Hewett 1 (Fig. 4). Alternatively, the counter-arc may be an expansion wave, where ionized gas in the tail of SDSO1 decelerates below the sound speed. In that case, the alternating waves of [O III] and Hα emission may correspond to pressure waves in the ionized gas tail of SDSO1.

The phenomenon of the GPN bow shock and tail is closely related to AGB wind bow shocks and tails (Young et al. 1993; Waters et al. 1994; Zijlstra & Weinberger 2002; Wareing et al. 2006b; Martin et al. 2007). In fact, the AGB progenitors of PNe and their winds are expected to shape the ISM and set the stage for PNe-ISM interactions (Wareing et al. 2007a). However, be-

cause of their much lower mass outflow rate, the standoff radii of AGB bow-shocks and their tail widths are typically much smaller than the scale of GPNe shells and tails. For example, the famous nearby AGB star Mira has a mass outflow rate of $10^{-7} M_{\odot}$, a bow-shock standoff radius of 0.1 pc, tail width of 0.8 pc, and observable tail length of 3.5 pc (Martin et al. 2007; Wareing et al. 2007b). That means that any future Mira PN shell will overtake and merge with the AGB wind bow-shock long before transitioning to the GPN stage. While AGB wind mass outflow rates are typically much lower than PN mass outflow rates, they last a much longer time (~ 0.5 Myr), and contain more mass than the PN shell. Interaction with the AGB wind may therefore considerably alter the PN shell mass, velocity, radial structure, and shape. In our analysis below, we will assume that the combined PN plus AGB wind incorporates the entire mass shed by the star. However, it is possible that a fraction of the stellar mass was left behind in the AGB tail. It may also be possible to detect the progenitor AGB tail as a narrower extension of the GPN tail in some cases.

4.5. *GPN Expansion and Energetics*

From the appproximate age, size, and mass of the SDSO1 GPN, we can estimate its initial expansion velocity and final size by assuming all of its kinetic energy goes into PdV work on the surrounding ISM, which has a density of $n_e = 0.02$ cm^{-3} and photoionization equilibrium temperature of $T = 10^4$ K (§4.3). We start the clock after the PN shell has swept up and incorporated the bulk of the mass of the AGB wind, and the combined wind begins to interact directly with the ISM. To first approximation, we assume roughly spherical expansion in the case that the ISM ram pressure in the forward direction is negligible. We also assume that the ongoing energy injection by EG And is negligible, based on its very weak mass outflow rate and negligible absorption of UV photons by the PN shell after its initial expulsion. Assuming a mass of $\sim 1 M_{\odot}$, we find that the GPN shell had an initial velocity of 27 km s^{-1} (Fig. 7) and kinetic energy of 7×10^{45} erg. The maximum radius obtainable by the SDSO1 GPN would then be 26 pc, consistent with its observed size of 20 pc. The ISM mass displaced by GPN expansion amounts to $\sim 6 M_{\odot}$, significantly greater than the GPN mass itself.

We find that a GPN shell in the low-density environment of SDSO1, within the mass range $0.7 - 2.0 M_{\odot}$, will decelerate its outward motion by 10% by the time it reaches a diameter of $\sim$ 15 pc. The maximum diameter of a GPN depends weakly on the external ISM pressure, as $P^{-1/3}$, varying by a factor of 2.1 for a factor of 10 in pressure. At its current age of 400 kyr, and assuming a mass of $\sim 1 M_{\odot}$ the SDSO1 GPN has slowed its expansion by 15% to 23 km s^{-1} and is approaching its maximum diameter of 26 pc. The mean power input to the ISM by the GPN expansion so far is 3×10^{32} erg s^{-1}, comparable to the mean power of 4×10^{32} erg s^{-1} injected over its 650 kyr expected lifetime. The lifetime mean power from the GPN deceleration along its direction of motion through the ISM is 20 times greater, at 6×10^{33} erg s^{-1} ($1.5 L_{\odot}$), comparable to the observed [O III] luminosity of $2.4 L_{\odot}$. It appears that much of this power is dissipated in line emission from the GPN-driven shock.

The preceding discussion applies when the ram pressure is negligible compared to the GPN expansion, which ceases to be true for fast-moving PNe at late times as the expansion velocity decelerates. The ratio of the pressure of the expanding PN shell to the ram pressure of the ISM is $P_{PN}/P_{ISM} = (n_{PN}/n_{ISM}) * (v_{e,PN}/v_{ISM})^2$. For an initial expansion velocity of 27 km s^{-1}, this ratio is greater than unity for $n_{PN} > 0.3$ cm^{-3}. In this regime, the GPN continues to expand and does not reach pressure equilibrium with the ISM wind in the forward direction until the expansion velocity drops below a density-dependent threshold. Until that time, the distance of the bow shock from EG And will follow Figure 7. After that time, the GPN will continue to expand laterally, but not in the forward direction, causing it to flatten into a prolate ellipsoid. After the GPN stops expanding, ram pressure from the ISM will decelerate the GPN, displacing it from EG And and stretching it into a lengthening tail as the star continues its forward motion, immune to ram pressure (Wareing et al. 2007a). The fact that EG And is well centered in the cavity behind the head of the Hα tails shows that the GPN has not yet entered this stage and must still be expanding.

4.6. *Photoionization by EG And*

EG And is still hot and luminous enough to photoionize the SDSO1 GPN and the surrounding ISM. While photons below the Lyman limit are subject to absorption, we find that the column density of the GPN shell is not enough to significantly impede the EUV flux. The size of the Stromgren sphere photoionized by EG And depends on its ionizing luminosity and the density of the surrounding ISM. The mean densities of ionized and neutral gas in a 40×40 pc box surrounding SDSO1 are ~ 0.02 cm^{-3} and ~ 0.004 cm^{-3}, respectively. The number of H-ionizing photons integrated over a 70,000 K blackbody with luminosity $10 - 90 L_{\odot}$ is $Q = \frac{4\pi}{3} r_1^3 n_H^2 \alpha_B = 1 - 9 \times 10^{45}$ photons, ionizing a Stromgren sphere out to distance of 15-31 pc from EG

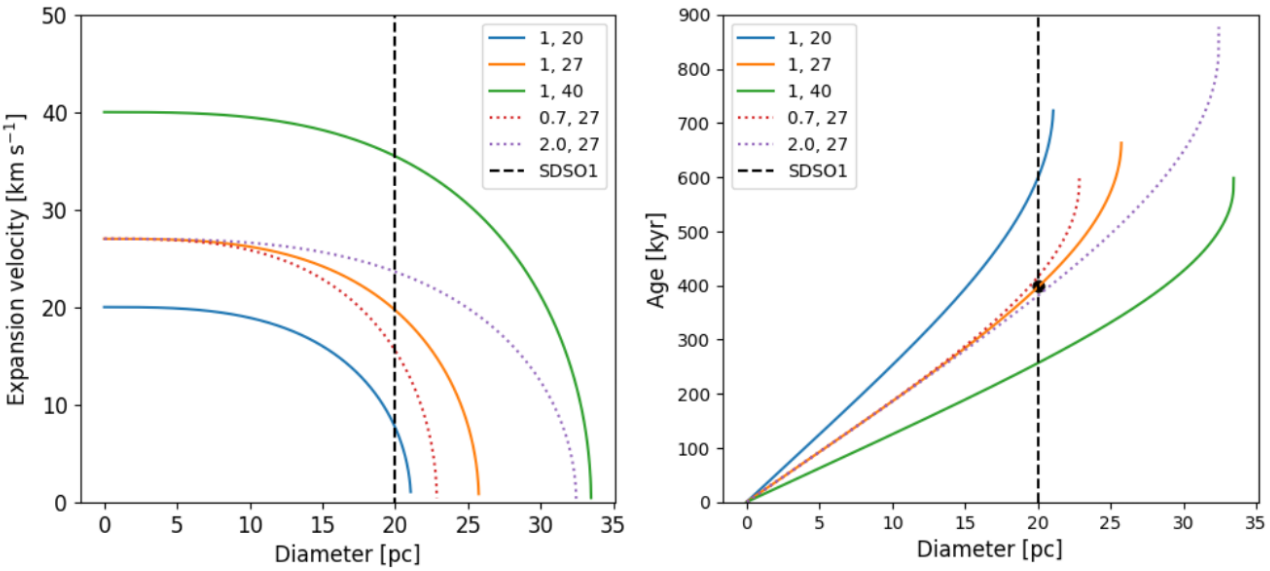

Figure 7. Expansion model for GPNe, assuming an outflow mass of $1M_{\odot}$ (solid lines) and that all of the initial kinetic energy goes into PdV work on the ISM. The expansion velocity decreases with time as the GPN shell does work. The dashed line and black circle mark the estimated diameter and age of the SDSO GPN. This model matches the observations for an initial expansion velocity of 27 km s^{-1}. The dotted lines show the effect of varying the mass of the PN shell between 0.7 and $2.0M_{\odot}$ for an initial velocity of 27 km s^{-1}. Based on this plot, PNe in this mass range will decelerate by $> 10\%$ by the time they reach a diameter of ~ 15 pc.

And (roughly twice the radius of the SDSO1 GPN). Note that the amount of mass expelled and displaced by EG And is negligible in this calculation, $< 3\%$ of the ISM mass within the Stromgren sphere.

We used Cloudy version 23.01 to model the photoionized spectrum of the SDSO1 GPN, assuming a mass of $2M_{\odot}$ is compressed into a spherical shell with thickness $\Delta R = 0.1 - 1.0$ pc. The actual thickness depends on the evolution of the GPN structure, including the effects of its hypersonic motion through the ISM. We assume an input black body spectrum from a WD with temperature 70 kK and luminosity $50L_{\odot}$. Typical planetary nebula elemental abundances are invoked, using the Cloudy command "abundances planetary nebula" (Aller & Czyzak 1983). For these parameters, we find that the model GPN shell is only partially ionized with $N(\mathrm{H+})/N(\mathrm{H_{tot}}) = 0.42$ - 0.62, yielding negligible [O III] emission, and an [O III]/Hβ ratio of 0.0030-0.047. Next we tried a filled spherical model, with constant density of 0.019 cm^{-3}, which turns out to be similar to the density of the surrounding ISM. In this case, the model PN shell is highly ionized, with $N(\mathrm{H+})/N(\mathrm{H_{tot}}) = 0.995$, yielding significant [O III] emission, and an [O III]/Hβ ratio of 4.8. However, the total [O III] flux of 9.0×10^{-13} erg s^{-1} cm^{-2} is spread out over the entire projected area of the PN and the mean surface brightness of photoionized [O III] emission from the SDSO1 PN (6.1×10^{-21} erg s^{-1} cm^{-2} arcsec^{-2}) is far below the detection limit of ground-based telescopes. This calculation emphasizes that large, old PNe and GPNe are undetectable even if the WD is still capable of ionizing them. The only reason that SDSO1 is detectable is that its hypersonic motion generates a strong shock and tail via its interaction with the ISM.

4.7. *Shock Models*

The morphology and strong [O III] emission from the SDSO1 arc are consistent with a GPN bow shock. Following Soker et al. (1991), the post-shock temperature for fully ionized gas is expected to be $3.45 \times 10^4 (v/50[km/s])^2 = 1.6 \times 10^5$ K for an GPN moving at 107 km s^{-1} and the cooling time is $\sim 100(v/50[km/s])^3/\beta n_0$ yr $= 49$ kyr for an equilibrium shock with $\beta = 1.0$. We used the MAPPINGS code (ver. 5.1) to generate a grid of 1-D shock models for velocities of 20-200 km s^{-1} and magnetic field $B = 0.001 - 1$ μG (Allen et al. 2008). We assume the shock propagates in photoionized gas with a density of 0.01 cm^{-3} and temperature of $T = 1.0 \times 10^4$ K, based on the ISM map of McCullough et al. (2001) in Figure 6. Case B is used to convert between Hα and Hβ fluxes, assuming no reddening.

The emission line ratios predicted by the shock models compare favorably to the observed emission line ratios in the SDSO1 arc (Fig. 8). The [O III]/Hβ emission line ratios in the highest ionization regions of SDSO1 are consistent with the models for the shock velocity of $\sim$ 100 km s^{-1} expected from the motion of EG And

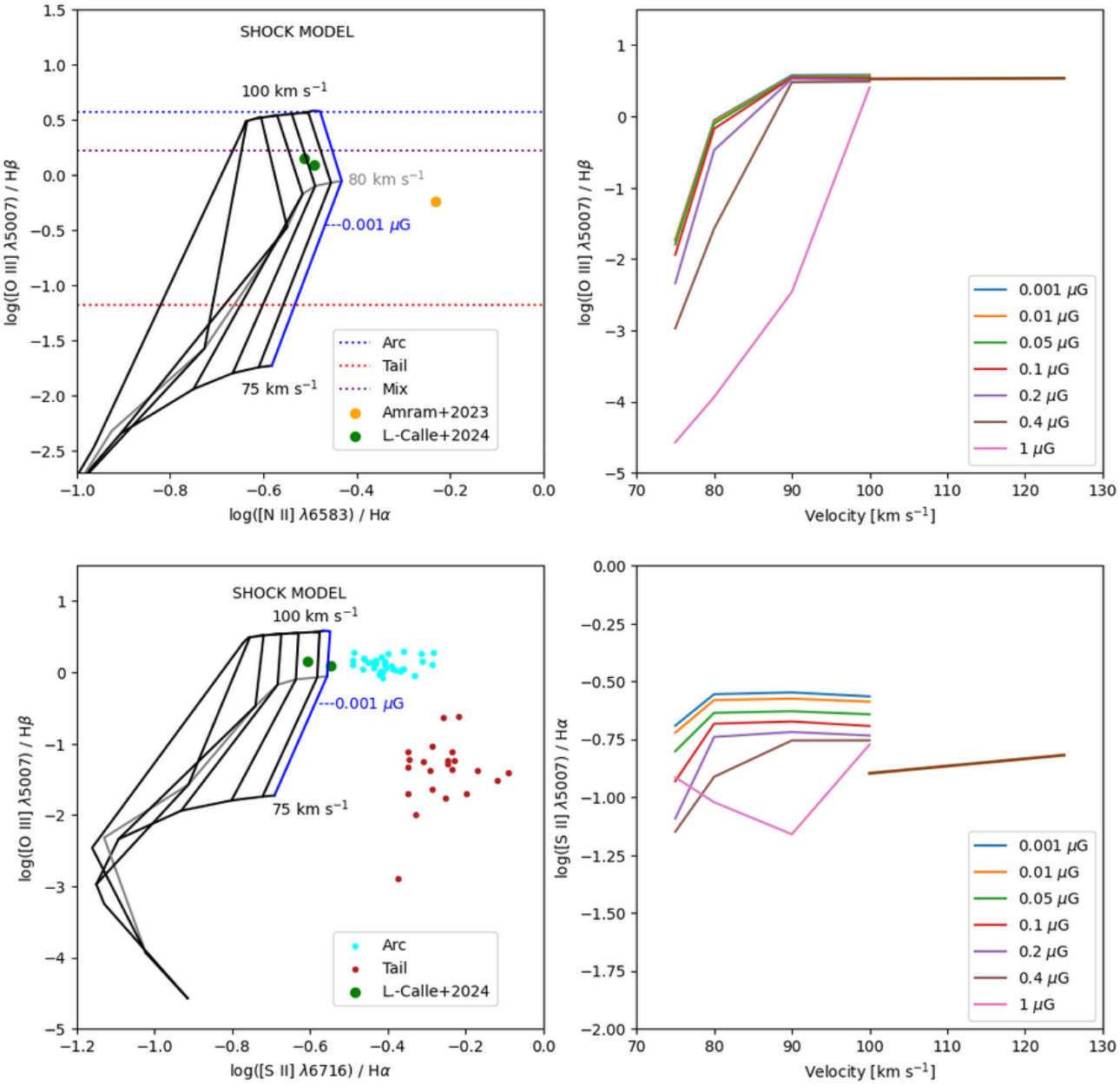

Figure 8. Emission line ratios in the SDSO1 arc and tail, compared to a grid of MAPPINGS models for a $v = 75 - 125$ km s^{-1} shock impinging on ISM with a pre-shock density of 0.01 cm^{-3}, solar abundance, and magnetic field of 0.001-1.0 μG. Photoionized precursor emission is not significant in this velocity range. The [O III]/Hβ ratios for our data are estimated from the observed [O III]/Hα assuming Case B recombination. We compare our results to the line ratios from Lumbreras-Calle et al. (2024) and Amram et al. (2023). Regions where the shock is projected in front of the tail have a mixed line ratio with lower ionization as a consequence of perspective. The [O III]/Hβ ratio plummets for shock velocities < 80 km s^{-1}. The [S II]/Hα ratio is somewhat suppressed at higher magnetic field.

relative to the local ISM. Most of the emission comes from the shock itself, while the shock precursor only has a small effect on the model at this velocity. The [S II]/Hα ratio is roughly a factor of 2 higher in the SDSO1 shock than predicted by the models. This might indicate a higher density shock or greater S abundance than assumed in the models. The [S II]/Hα ratio is also enhanced where both the arc and tail cross the line of sight, as a consequence of projection. The Hα tail has much lower ionization as traced by [O III]/Hβ, possibly originating as dense gas ablated from the GPN and heated by mixing with or conduction from the shocked ISM. Alternatively, this may be a signature of post-shock cooling and recombination.

4.8. *SDSO1 Bow Shock Structure and Kinematics*

SDSO1 does not show a strong [O III] peak in the direction of motion, but rather a relatively uniform cap, modulated by waves of emission. Because the [O III] surface brightness is not strongly concentrated, it is difficult to accurately locate the tip of the bow shock. Similar structure is found in the A66 15 GPN candidate (Fig. 4). In both nebulae, the sharp rear edge of the bow shock may demark the line where the velocity drops below the $\sim$ 80 km s^{-1} needed to produce strong [O III] emission. Note that this structure might be smeared out by the relative motions of post-shock gas on the 49 kyr cooling timescale, corresponding to 2.5 pc (0.2 deg) in the plane of the sky. The multiple striations in SDSO1 are reminiscent of the striations seen in the Pencil nebula, a part of the Vela supernova remnant. These striations may indicate sound waves propagating through the ionized gas or compression along magnetic field lines. Turbulence across the face of the bow shock can corrugate its surface and lead to vortex shedding like what is seen in the Firefox nebula Sh 2-188 (Wareing et al. 2006a). The wavy features in the Hα tail of SDSO1 look similar to this and may derive from turbulence driven by the Kelvin-Helmholtz instability across the bow shock. However, since turbulence can be suppressed at high Mach number near the head of the bow shock, these features may arise from slower, downstream regions of the oblique shock.

Amram et al. (2023) measure the SDSO1 radial velocity to be -96 ± 4 km s^{-1}, which is consistent with EG And, albeit at a relatively low spectral resolution. However, other spectra of the brightest [O III] emission from SDSO1, taken from locations near its trailing edge, indicate radial velocities of -6 to -34 km s^{-1}(Fesen et al. 2023; Lumbreras-Calle et al. 2024), which are quite different from the radial velocity of EG And. At the head of the bow shock where the postshock gas has been accelerated to the velocity of the GPN and the shock heating is the greatest, the maximum velocity should match the -107 km s^{-1} velocity of the GPN with respect to the ISM and -95 km s^{-1} radial velocity of EG And, plus the residual radial expansion velocity of -20 km s^{-1} . However, the velocity of the bow shock is expected to decrease away from this location and should therefore be lower elsewhere in SDSO1. For example, at the sonic line, the postshock velocity might only be -15 km s^{-1} and the projected velocity -13 km s^{-1}, consistent with the values measured by Lumbreras-Calle et al. (2024). It will therefore be important to sample the kinematics of SDSO1 at more locations across the bow shock in order to resolve the issue of the existing, possibly discrepant radial velocity measurements, and to understand its dynamics better.

4.9. *Statistics and Fates of the Old PNe and GPNe Populations*

Having identified several candidate GPNe, we consider their importance for late-stage PNe evolution. The local WD birth rate density is estimated to be $\chi_{\rm WD} = (1.00 \pm 0.25) \times 10^{-12}$ pc^{-3} yr^{-1} (Liebert et al. 2005). Assuming that most of these WD launch PNe that are observable for 20 kyr, and a PNe scale height of 220 ± 25 pc (Frew 2008), then the local PN surface density is expected to be 8.8 kpc^{-2}. It follows that there should be $\sim$ 62 PNe associated with WD that have $D < 1.5$ pc and ages < 20 kyr within 1.5 kpc of the sun. Empirically, there are 68 PNe within 1.5 kpc with $D < 1.5$ pc that have Gaia DR3 parallax measurements of their central star, from the catalog of Chornay & Walton (2021), closely matching this expectation. Scaling the observed number by age, we expect there to be 272 old PNe with $D = 1.5 - 9$ pc and expansion ages of 20-100 kyr in this volume. However, there are only 67 in our list, compiled by cross-matching the HASH database with Gaia DR3 parallaxes (Table 2). We appear to be missing 75% of nearby old PNe, which remain to be discovered, are effectively invisible because they have faded and are not interacting strongly with the ISM, or have already been stripped by an interaction with dense ISM. Depending on their survival rate, there may be as many as 1300 GPNe with expansion ages of 100-400 kyr in the same volume, but we have so far only identified six in this age range (0.5%). Because their photoionized emission fades below detectability as they grow, we expect that the observability of old PNe and GPNe depends on their velocity with respect to and interaction with the ISM. Consistent with this expectation, roughly half of old PNe (32/66) have transverse or radial velocities > 30 km s^{-1} and 27/66 have obvious interaction sig-

natures, such as a shock-tail morphology. Furthermore, seven have measured radial velocities with $v_r > 55$ km s^{-1}, approaching the ISM velocity required to generate copious [O III] emission in a shock. It will be important to measure radial velocities for more central stars of old PNe to test this idea further.

According to Fig. 7, GPNe slow their expansion by 10-50% by the time they reach an age of 200-600 kyr. Within 600-700 kyr they expand to a terminal diameter of 20-35 pc, expend all of their outflow kinetic energy, and stop expanding completely. Mixing of a GPN with the ISM is accomplished by ram-pressure stripping once it has stopped expanding. An expansion shock is driven through the GPN in a cloud-crushing time of ~ 1 Myr as it decelerates its expansion, disrupting and fragmenting it. However, given the short cooling time, the remnant can persist up to 10 Myr (Scannapieco & Brüggen 2015), leaving a kpc-long trail as it continues to moves through the ISM. Given the abundance of GPNe, we predict that thousands of GPNe trails may be found in sky, perhaps explaining some of the long linear features seen in all-sky Hα surveys (Haffner et al. 1998, 2003). In addition to this motion, the progenitor star will orbit the Galaxy several times and can move a large radial distance during its lifetime if given either a kick in its natal cluster or later by a companion that goes supernova. High-velocity stars can thereby serve to transport metals outward in the Galaxy disk (Johnson et al. 2021) and deposit them in the ISM via AGB + PNe outflows.

Table 2. Large GPNe and PNe

Nebula	Central Star	v_t, v_r	d	Θ	D	Age	Morph.
		[km s^{-1}]	[pc]	[']	[pc]	[kyr]	
GPN Candidates							
NGC 7094 Halo	WD 2134+125	89, -1	1655	75	36	418	shock
PN A66 15 Halo	WD 0625-253	182, ···	6042	20	35	407	shock-tail
SDSO 1	EG And	52,-95	608	113	20	232	shock-tail
Alves 2	Gaia DR3 957591309724015872	210, ···	1359	40	16	183	shock-tail
MWP 1 Halo	WD 2115+339	29, ···	502	78	11	132	shock
NGC 3242 Halo	GALEX J102446.3-183834	30,4.7	1342	90	9	105	FUV shock-tail
EGB 10 Halo	TYC 4454-1299-1	31, 16	290	72	6.1	70	shock
Hewett 1	PG 1034+001	85, 65	193	60	3.4	39	shock-tail
Large, Old PNe ($D > 1.5$ pc)							
PN PaStDr 9 (Titan)	FBS 0212+385	36, 4	310	90	8.1	94	shock-tail
WPS 62	WD 0444+049	53, ···	440	60	7.7	89	
WPS 75	GALEX J095422.9-050209	79, ···	401	60	7.0	81	
WPS 46 (Vulcan)	PG 0931+691	23, ···	580	38	6.5	75	shock
Ton 320	PG 0823+317	38, 42	551	39	6.3	73	
WPS 54	PG 0948+534	44, 95	315	60	5.5	64	
Fr 2-30	UCAC4 686-007194	66, ···	890	23	6.0	69	
PN StDr 56 (Goblet)	LAMOST J020717.41+300511.6	34, 88	421	44	5.4	62	
Pa J0637.4+3327	GALEX J063728.2+332706	7, ···	1050	16	4.9	57	shock-tail
EC 13290-1933	GALEX J133146.3-194825	76, ···	1245	13	4.7	54	
Fr 2-16	WD 2115+118	11, ···	520	30	4.5	53	
Fr 2-21	PHL 4	184, ···	1636	9.0	4.3	50	
PN AlvKn 1	GALEX J080404.4-063058	23, ···	824	17	4.0	47	shock
BMP J0733-3108	GALEX J073324.2-310804	28, ···	1175	12	4.0	46	

Table 2 *continued*

Table 1. Observations

Band	Integrated Exposure Time
Wide-field imaging	
Five telescopes: f/5 Takahashi FSQ106 EDX4 at f/3.6 or f/3	
Cameras: ZWO ASI6200MM Pro, ASI2600MM Pro, ASI 6200MM; QHYCCD QHY600M, Zeus 455M Pro	
Narrow band Filters: Antlia & Chroma 3 nm bandpass S, H, O	
Broad band Filters: Antlia, Chroma, & Astrodon R, G, B	
[O III]	312.8
Hα	148.1
R	18.5
G	16.5
B	29.5
Total	525.4
Narrow-field imaging	
Telescopes: APM Apo 107/700, Askar FRA600, Celestron C9.25 SC XLT, Celestron RASA 8",	
CFF Telescopes Refractor 135mm f/6.7, Sky-Watcher Equinox 80, Sky-Watcher Esprit 100ED,	
Sky-Watcher Esprit 150ED, Stellarvue SVX130T, Stellarvue SVX90T, Takahashi FSQ-106EDX4,	
TS-Optics Photoline 140mm f/6.5, William Optics Fluorostar 120 / FLT120,	
William Optics Fluorostar 132 / FLT132, William Optics ZenithStar 81 / ZS81	
Cameras: QHYCCD QHY268 M, QHY600PH M; RisingCam ATR3-26000KMA; ZWO ASI2600MC Pro,	
ASI2600MM Pro, ASI294MM Pro, ASI6200MM Pro	
Narrow band Filters: Various 3-5 nm bandpass S, H, O	
Broad band Filters: Chroma R, G, B	
[O III]	487.8
Hα	314.1
[S II]	168.9
R	17.3
G	26.3
B	15.6
Total	1030.0

Table 2 *(continued)*

Nebula	Central Star	v_t, v_r	d	Θ	D	Age	Morph.
		[km s^{-1}]	[pc]	[']	[pc]	[kyr]	
PN IsWe 2	WD 2212+656	13, ···	819	16	3.8	44	tail
Sh 2-216	WD 0439+466	16, 58	128	100	3.7	43	shock
Sh 2-176	WD 0029+571	14, ···	1110	11	3.6	41	shock-tail
PN StDr 138	GALEX 033755.8+434415	23, ···	979	12	3.4	40	
PN Dr 21	Gaia DR3 1938255660503776000	12, ···	1543	7.5	3.4	39	
Sh 2-188 (Firefox)	WD 0127+581	32, ···	943	12	3.2	37	shock-tail
PFP 1	Gaia DR3 3058094200264637312	24, ···	534	19	3.0	34	
PN CaVa 1	Gaia DR2 3158200679523220096	22, ···	1257	8.0	2.9	34	
PN WeDe 1	WD 0556+106	4, ···	580	17	2.9	33	tail

Table 2 *continued*

Table 2 *(continued)*

Nebula	Central Star	v_t, v_r	d	Θ	D	Age	Morph.
		[km s^{-1}]	[pc]	[']	[pc]	[kyr]	
BMP J1759-3321	Gaia DR3 4042513447762858880	11, ···	880	11	2.9	33	
EGB 6	WD 0950+139	56, ···	752	13	2.8	33	shock
PN PaStDr 3	GALEX J011928.8+490109	25, -28	807	12	2.8	33	
PN HDW 3 (Tiara)	WD 0322+452	30, ···	916	10	2.8	32	shock-tail
PN StDr 43	Gaia DR3 2005036900103208704	27, ···	1301	7.0	2.6	31	
PN A66 74	WD 2114+239	15, ···	658	13.8	2.6	31	
BMP J1808-1406	Gaia DR3 4146962654265880064	11, ···	1007	9.0	2.6	31	
PN StDr 13	GALEX J063422.6+072220	26, ···	1195	7.5	2.6	30	
PN Dr 27	GALEX J001103.6+571036	17, ···	992	9.0	2.6	30	
Sh 2-290 (PN A66 31)	GALEX J085413.0+085354	34, ···	543	16	2.6	30	shock
PN StDr 140 (Lori's)	GALEX J074320.3+160752	43, ···	1233	6.9	2.5	29	
PN PuWe 1	WD 0615+556	41, ···	395	21	2.4	27	
PN MeWe 2-4	GALEX J140115.5-504010	59, ···	1159	7.0	2.4	29	
PN Dr 24	Gaia DR2 1822392423722386482	35, ···	1269	6.4	2.4	27	tail
PHR J1625-4523	Gaia DR3 5942477172668108032	11, ···	1475	5.5	2.4	27	
PN A66 29	GALEX J084019.0-205435	21, ···	1064	7.6	2.3	27	
PN Kn 121	GALEX J20420.18+135116	48, ···	1278	6.0	2.2	26	shock-tail
PN Kn 63	Gaia DR3 3320608713128049280	26, ···	1304	5.9	2.2	26	shock
Sh 2-78	WD 1900+140	13, ···	698	10.9	2.2	26	tail
PN Falls 1 (Eye of Ibad)	UCAC4 280-014527	49, ···	749	10	2.2	25	
PN Alv 1	Gaia DR3 1866922365452368768	33, ···	1650	4.5	2.2	25	
PN A66 21 (Medusa)	WD 0726+133	26, ···	592	12.5	2.2	25	shock-tail
PN G341.5+12.1 (WR 72)	Gaia DR3 6010805807350513920	31, -92.5	1225	6.0	2.1	25	
Jacoby 1	PG 1520+525	45, ···	772	9.5	2.1	25	
PN Fal 2 (Cosmic Egg)	KPD 2045+5136	44, ···	1070	6.8	2.1	25	shock-tail?
IPHASX J055226.2+323724	GALEX J055226.1+323724	27, 11	981	7.4	2.1	27	
PN StDr 20 (Aurore's)	Gaia DR3 3028738476748576768	27, ···	1176	6.0	2.1	24	shock
MWP 1 (Methuselah)	WD 2115+339	29, ···	502	14	2.0	24	shock
PN A66 7	WD 0500-15	14, ···	517	13	2.0	23	
Fr 2-23	KPD 0311+4801	7, ···	231	28	1.9	21	
FP J1824-0319	UCAC4 434-076255	23, ···	195	32	1.8	21	shock
PN JnEr 1 (Headphones)	WD 0753+535	6, ···	939	6.6	1.8	21	
PN Lo 1	GALEX J025658.5-441016	98, ···	808	7.5	1.8	20	
PN K2-2	Gaia DR3 3158419684195782656	35, 57	830	7.3	1.8	20	
PN A66 66	Gaia DR3 6864496115795567488	45, ···	1148	5.2	1.7	20	
HFG 1	V664 Cas	32, ···	708	8.3	1.7	20	shock-tail
PN PaGo 2	GALEX J174415.3+223627	53, ···	594	10	1.7	20	tail
PN Jn 1	WD 2333+301	15, ···	989	5.9	1.7	20	
PN StDr 98	UCAC4 730-098595	14, ···	292	19	1.6	19	shock
PN IsWe 1	WD 0345+498	40, ···	425	12.5	1.5	18	tail

Table 2 *continued*

Table 2 *(continued)*

Nebula	Central Star	v_t, v_r	d	Θ	D	Age	Morph.
		[km s^{-1}]	[pc]	[']	[pc]	[kyr]	
Alves 5	GALEX J171241.6+015533	17, ···	885	6.0	1.5	17	
Sh 2-174 (Valentine Rose)	GD 561	39, ···	290	18	1.5	17	shock-tail

5. CONCLUSIONS

Our deep narrowband imaging supports a picture where SDSO1 is a bow shock driven by the virtually invisible, hypersonic SDSO1 GPN into the ISM. We identify the central star of the GPN as EG And, a symbiotic WD binary at a distance of 608 pc from the sun. The GPN itself has expanded to a diameter of 20 pc, leading to an undetectably low nebular surface brightness from WD-photoionized emission. The emission we do see comes from a 107 km s^{-1} shock driven by the motion of the GPN through the ISM. The optical emission line ratios are dominated by the shock, with a minor to insignificant contribution from a photonionzed precursor. Long tails of Hα emission trace the turbulent trail of shocked ISM left behind by the GPN. Faint filaments of [O III] emission found just downstream of EG And may arise in the backflow region behind the GPN. The shock-tail morphology seems to be prevalent in old PNe, which may similarly only be detectable because of their interaction with the ISM.

SDSO1 is the first recognized member of a new class of shock-powered ghost planetary nebulae (GPNe), which are only visible by virtue of their interaction with the interstellar medium. We identify eight candidate members of the class, including five with diameters > 10 pc that have likely entered a final phase, where the outflow has decelerated significantly. These GPN are in the terminal stage of their evolution, having nearly reached their maximum diameter and will soon begin to be ram-pressure stripped and eventually encorporated the surrounding interstellar medium. Several GPN candidates present as giant halos surrounding much younger PNe, suggesting that there were two PN outflows launched 100-400 kyr apart, possibly from a pair of post-AGB stars that have now become a double-degenerate WD binary. It will be important to spectroscopically confirm or refute the presence of a binary central star in these systems, in order to test this scenario.

A significant portion of the data taken for this paper was obtained at Saturn Lodge observatory, adjacent to the Polaris Observatory Association. Saturn Lodge observatory is financially supported by RMR and MP. We thank the Deep Sky Collective for providing their deep narrow-band imaging that was crucial for measuring the emission line ratios in SDSO1. We thank the NHZ astrophotography collaboration for sharing their deep narrowband imaging of PN A66 15 and Bray Falls for sharing his deep narrowband imaging of Hewett 1. Many thanks to Mark Wareing for reading and discussion about PN-AGB wind interactions. This work has made use of data from the European Space Agency (ESA) mission *Gaia* (https://www.cosmos.esa.int/gaia), processed by the *Gaia* Data Processing and Analysis Consortium (DPAC, https://www.cosmos.esa.int/web/gaia/dpac/consortium). Funding for the DPAC has been provided by national institutions, in particular the institutions participating in the *Gaia* Multilateral Agreement. This research has made use of the SIMBAD database, operated at CDS, Strasbourg, France. This research has made use of the NASA/IPAC Extragalactic Database (NED), which is funded by the National Aeronautics and Space Administration and operated by the California Institute of Technology.

Facilities: Gaia

Software: astropy (Astropy Collaboration et al. 2013, 2018), Cloudy (Ferland et al. 2013), MAPPINGS

REFERENCES

Allen, M. G., Groves, B. A., Dopita, M. A., Sutherland, R. S., & Kewley, L. J. 2008, ApJS, 178, 20, doi: 10.1086/589652

Aller, L. H., & Czyzak, S. J. 1983, ApJS, 51, 211, doi: 10.1086/190846

Amram, P., Adami, C., Epinat, B., & Chemin, L. 2023, A&A, 671, L13, doi: 10.1051/0004-6361/202346311

Astropy Collaboration, Robitaille, T. P., Tollerud, E. J., et al. 2013, A&A, 558, A33, doi: 10.1051/0004-6361/201322068

Astropy Collaboration, Price-Whelan, A. M., Sipőcz, B. M., et al. 2018, AJ, 156, 123, doi: 10.3847/1538-3881/aabc4f

Balick, B., Gonzalez, G., Frank, A., & Jacoby, G. 1992, ApJ, 392, 582, doi: 10.1086/171458

Borkowski, K. J., Sarazin, C. L., & Soker, N. 1990, ApJ, 360, 173, doi: 10.1086/169106

Boumis, P., Meaburn, J., Lloyd, M., & Akras, S. 2009, MNRAS, 396, 1186, doi: 10.1111/j.1365-2966.2009.14784.x

Chiotellis, A., Boumis, P., Nanouris, N., Meaburn, J., & Dimitriadis, G. 2016, MNRAS, 457, 9, doi: 10.1093/mnras/stv2798

Chornay, N., & Walton, N. A. 2021, A&A, 656, A110, doi: 10.1051/0004-6361/202142008

Corradi, R. L. M., Schönberner, D., Steffen, M., & Perinotto, M. 2003, MNRAS, 340, 417, doi: 10.1046/j.1365-8711.2003.06294.x

Drechsler, M., Strottner, X., Sainty, Y., et al. 2023, Research Notes of the American Astronomical Society, 7, 1, doi: 10.3847/2515-5172/acaf7e

Edenhofer, G., Zucker, C., Frank, P., et al. 2024, A&A, 685, A82, doi: 10.1051/0004-6361/202347628

Ferland, G. J., Porter, R. L., van Hoof, P. A. M., et al. 2013, RMxAA, 49, 137. https://arxiv.org/abs/1302.4485

Fesen, R. A., Kimeswenger, S., Shull, J. M., et al. 2023, ApJ, 957, 82, doi: 10.3847/1538-4357/acfe0d

Fragkou, V., Parker, Q. A., Zijlstra, A. A., et al. 2022, ApJL, 935, L35, doi: 10.3847/2041-8213/ac88c1

Frew, D. J. 2008, PhD thesis, Macquarie University, Department of Physics and Astronomy

Frew, D. J., Parker, Q. A., & Bojičić, I. S. 2016, MNRAS, 455, 1459, doi: 10.1093/mnras/stv1516

Haffner, L. M., Reynolds, R. J., & Tufte, S. L. 1998, ApJL, 501, L83, doi: 10.1086/311449

Haffner, L. M., Reynolds, R. J., Tufte, S. L., et al. 2003, ApJS, 149, 405, doi: 10.1086/378850

Heckathorn, J. N., Fesen, R. A., & Gull, T. R. 1982, A&A, 114, 414

Hewett, P. C., Irwin, M. J., Skillman, E. D., et al. 2003, ApJL, 599, L37, doi: 10.1086/381139

Jacob, R., Schönberner, D., & Steffen, M. 2013, A&A, 558, A78, doi: 10.1051/0004-6361/201321532

Johnson, J. W., Weinberg, D. H., Vincenzo, F., et al. 2021, MNRAS, 508, 4484, doi: 10.1093/mnras/stab2718

Kenyon, S. J., & Garcia, M. R. 2016, AJ, 152, 1, doi: 10.3847/0004-6256/152/1/1

Liebert, J., Bergeron, P., & Holberg, J. B. 2005, ApJS, 156, 47, doi: 10.1086/425738

Lumbreras-Calle, A., Fernández-Ontiveros, J. A., Infante-Sainz, R., et al. 2024, arXiv e-prints, arXiv:2412.08327, doi: 10.48550/arXiv.2412.08327

Martin, D. C., Seibert, M., Neill, J. D., et al. 2007, Nature, 448, 780, doi: 10.1038/nature06003

McCallum, L., Wood, K., Benjamin, R. A., et al. 2025, MNRAS, doi: 10.1093/mnrasl/slaf023

McConnachie, A. W., Irwin, M. J., Ibata, R. A., et al. 2009, Nature, 461, 66, doi: 10.1038/nature08327

McCullough, P. R., Bender, C., Gaustad, J. E., Rosing, W., & Van Buren, D. 2001, AJ, 121, 1578, doi: 10.1086/319409

Ransom, R. R., Kothes, R., Geisbuesch, J., Reich, W., & Landecker, T. L. 2015, ApJ, 799, 198, doi: 10.1088/0004-637X/799/2/198

Scannapieco, E., & Brüggen, M. 2015, ApJ, 805, 158, doi: 10.1088/0004-637X/805/2/158

Soker, N., Borkowski, K. J., & Sarazin, C. L. 1991, AJ, 102, 1381, doi: 10.1086/115963

Tweedy, R. W., & Kwitter, K. B. 1994, AJ, 108, 188, doi: 10.1086/117057

—. 1996, ApJS, 107, 255, doi: 10.1086/192364

Tweedy, R. W., Martos, M. A., & Noriega-Crespo, A. 1995, ApJ, 447, 257, doi: 10.1086/175871

van Buren, D., Noriega-Crespo, A., & Dgani, R. 1995, AJ, 110, 2914, doi: 10.1086/117739

Van Dyke, M. 1982, An Album of Fluid Motion (Parabolic Press)

Wareing, C. J., O'Brien, T. J., Zijlstra, A. A., et al. 2006a, MNRAS, 366, 387, doi: 10.1111/j.1365-2966.2005.09875.x

Wareing, C. J., Zijlstra, A. A., & O'Brien, T. J. 2007a, MNRAS, 382, 1233, doi: 10.1111/j.1365-2966.2007.12459.x

Wareing, C. J., Zijlstra, A. A., O'Brien, T. J., & Seibert, M. 2007b, ApJL, 670, L125, doi: 10.1086/524407

Wareing, C. J., Zijlstra, A. A., Speck, A. K., et al. 2006b, MNRAS, 372, L63, doi: 10.1111/j.1745-3933.2006.00227.x

Waters, L. B. F. M., Loup, C., Kester, D. J. M., Bontekoe, T. R., & de Jong, T. 1994, A&A, 281, L1

Wilson, R. E. 1950, PASP, 62, 14, doi: 10.1086/126211

Young, K., Phillips, T. G., & Knapp, G. R. 1993, ApJ, 409, 725, doi: 10.1086/172702

Zijlstra, A. A., & Weinberger, R. 2002, ApJ, 572, 1006, doi: 10.1086/340438